Theoretical Exploration of Structural and Excitonic Properties in Black Phosphorus: From First-Principles to a Semi-Empirical Approach

Diego Guedes-Sobrinho,* Celso R. Caldeira Rêgo,* Gabriel Reynald Da Silva, Henrique R. Da Silva, W. Wenzel, Maurício J. Piotrowski,* and Alexandre Cavalheiro Dias*

ABSTRACT: Black phosphorus serves as an exemplary stacked bidimensional semiconductor, exhibiting anisotropic features in electronic and optical properties that demand special attention in theoretical investigations. Herein, we employed a series of computational protocols, starting with first-principles approaches (particularly density functional theory—DFT), combined with the solution of the Bethe−Salpeter equation within the tight-binding method to explore the structural stability and optoelectronic properties (bandgap, exciton binding energies, and optical absorption) of black phosphorus (P_n) across layers ranging from n = 1 to 6 and bulk. In our DFT investigations, we observed that empirical and semiempirical van der Waals models, contributing a dispersion energy component, revealed a myriad of differences and similarities in properties, such as interlayer nonbonded interactions. Notably, the many-body dispersion correction exhibited superior performance in connecting layered systems with the bulk. The magnitude of dispersion energies correlated with the stability during the aggregation process $P_{(n-1)} + P_1 \rightarrow P_n$. Additionally, the bandgap, properly corrected through relativistic quasi-particle calculations, narrowed due to enhanced interlayer wave function overlap, a result of the dispersion energies promoting the shortening of interlayer distances. Subsequently, we utilized the band structure relativistically corrected as a starting point to obtain the Hamiltonian, achieved through the generation of maximally localized Wannier functions. This facilitated a screening of the electron−hole (e−h) pairwise interaction Coulomb potential, specifically the exciton binding energy. We identified an indirect impact of the dispersion energies on excitonic properties, which were effectively described by the Rytova−Keldysh model for the e−h Coulomb potential, aligning well with photoluminescence experiments.

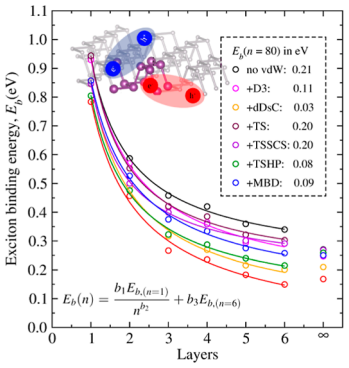

1. INTRODUCTION

Since 2014, when it was first proposed as a channel material for field-effect transistor (FET) applications by Li et al.,[1] black phosphorus (BP) has captured the attention of the two-dimensional (2D) semiconductor materials community.[2−7] Arranged in a puckered honeycomb lattice (orthorhombic, space group *Cmca*), phosphorus atoms introduce in-plane anisotropy across electrical, optical, thermal, and mechanical characteristics. This distinctive profile positions BP not only as a promising material for FET applications[8,9] but also for a myriad of electronic and photonic applications.[10−12] However, due to its nature as multilayers weakly interacting through van der Waals (vdW) forces—similar to graphene and achievable through mechanical exfoliation of bulk material[13]—the computational design of bandgap and excitonic properties, achieved by controlling the layer number, necessitates a precise description of interlayer interactions. Additionally, the impact of the chosen theoretical approach on predicting BP properties should be carefully considered.

Experimental findings have consistently reported a sizable dependence of the BP bandgap on layer thickness. This dependence exhibits an exponential decrease, ranging from approximately 2.0 eV for monolayers to 0.30−0.40 eV for the bulk.[14−17] Simultaneously, the carrier mobility undergoes significant changes, varying within the interval of 1000−10,000 $cm^2/V{\cdot}s$ from monolayer to bulk.[7,8,18] This underscores the challenge of spatial confinement effects on optoelectronic features, particularly the exciton energy spectrum, where information regarding electron−hole (e−h) interactions is captured.[19−21] In this context, computational design based on ab initio calculations, particularly through density functional theory (DFT), has been instrumental in providing crucial insights into the electronic−atomistic interface.[22−26] However, standard DFT studies employed to investigate BP systems face certain limitations of the typical exchange−correlation (*xc*) functionals used in crystal solids. These limitations include: (i)

the underestimation of bandgap energies[27,28] and (ii) the inadequate description of vdW interactions among BP interlayers, currently inserted via the $E_{KS+vdW} = E_{KS} + E_{disp}$ relationship,[29,30] wherein E_{KS} is the standard Kohn–Sham (KS) energy and E_{disp} is the vdW dispersive energy obtained *a posteriori* through vdW correction models.

The E_{disp} is accepted as an improvement of the standard DFT approach when just the E_{KS} is considered. At this context, several vdW models have been proposed to E_{disp} calculation, such as the most known empirical class proposed by Grimme,[31−33] which is based on the addition of the coordination number dependence (named D3)[34] as well as its version by replacing the damping function by the Becke–Johnson (BJ) model (D3BJ).[35] A representative semiempirical models are based on the set of Tkatchenko–Scheffler (TS) methods, composed by the simplest TS model as dependent on the charge density (but considering some parametrized terms),[36] TS by including self-consistent screening (named by TSSCS),[37,38] TS model based on iterative Hirshfeld partitioning (TSHP),[39,40] and the many body dispersion (MBD).[37] Another semiempirical method is the Steinmann approach[41,42] also density-dependent (named by dDsC) from the generalized gradient approximation through dipole moment calculation.

While the BP excitonic properties in mono- and few-layer systems hold crucial significance for optoelectronic device applications, understanding the influence of a substrate or the effects of layer stacking on exciton binding energy calculations remains inconclusive. For example, quasi-particle (QP) calculations within the GW approach have unveiled the suppression of BP binding energy (E_b) from $n = 1 \rightarrow 4$ layers due to the environmental screening effects of hexagonal boron nitride (hBN) and sapphire.[43] Conversely, even with the state-of-the-art GW method, known for capturing many-body effects, its prohibitive computational cost limits systematic studies involving large systems. For BP monolayers as freestanding systems, the calculated E_b = 0.48 eV was found to be underestimated compared to the experimentally reported value of 0.9 ± 0.1 eV obtained via polarization-resolved photoluminescence (PR–PL).[16] Consequently, exploring computationally more economical alternatives within DFT approaches becomes crucial to understanding how several vdW methods operate in BP and their impact on structural, electronic, and optical properties.

In this study, we systematically investigate the impact of several empirical and semiempirical vdW methods on the optoelectronic properties of BP (P_n), ranging from n = 1, 2, 3, 4, 5, 6 up to bulk. The structures are optimized using vdW-based methods, and we employ the computationally efficient relativistic QP correction known as DFT-1/2,[44] to calculate bandgap energies within a single-particle theory. Utilizing the DFT-1/2 bandgap as a starting point, we proceed to calculate excitonic properties through the solution of the Bethe–Salpeter equation (BSE) within a tight-binding (TB) approach. Our methodology involves employing the maximally localized Wannier functions TB (MLWF-TB) approach to derive the orthogonal TB Hamiltonian. This Hamiltonian is then used for a comprehensive screening of a set of 2D and 3D Coulomb potentials, providing a detailed description of the exciton e–h interaction.

2. THEORETICAL APPROACH AND COMPUTATIONAL DETAILS

Our sequential calculation protocol, depicted in Figure 1, follows a systematic strategy:

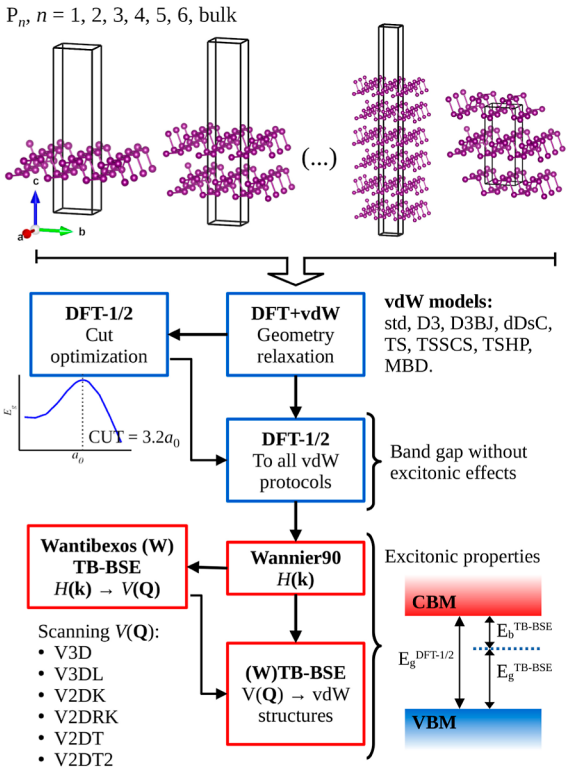

Figure 1. Sequential protocol for calculating excitonic properties in BP (P_n) systems (n = 1, 2, 3, 4, 5, 6, and ∞). DFT calculations were carried out using the VASP code, followed by the utilization of Wannier90 to derive the TB Hamiltonian. This Hamiltonian was then incorporated into the WanTiBEXOS code for the computation of excitonic properties.

- Ab initio geometry relaxation: perform ab initio calculations for geometry relaxations of multilayer BP systems, denoted as P_n, where n = 1, 2, 3, 4, 5, 6, and ∞ (bulk). Utilize several empirical and semiempirical vdW corrections ($E_{tot} = E_{KS} + E_{disp}$), such as D3, D3BJ, dDsC, TS, TSSCS, TSHP, and MBD. The detailed descriptions can be found in the Supporting Information.
- Relativistic QP correction (DFT-1/2): optimize the cut function within the DFT-1/2 method to prevent interpenetration between neighboring atoms. Determine the CUT parameter variationally for bandgap calculations in mono- and bilayers, maximizing the gap energy without empirical parameters.
- DFT-1/2 bandgap calculations: perform DFT-1/2 calculations for bandgaps without excitonic effects for all P_n systems obtained from the optimized vdW-based methods.
- MLWF-TB: employ the MLWF-TB approach to calculate the orthogonal TB Hamiltonian, denoted as $H(\mathbf{k})$. This Hamiltonian is obtained through the Wannier90 package[45] and serves as input for the WanTiBEXOS (W) code,[46] which handles QP effects and optical properties.

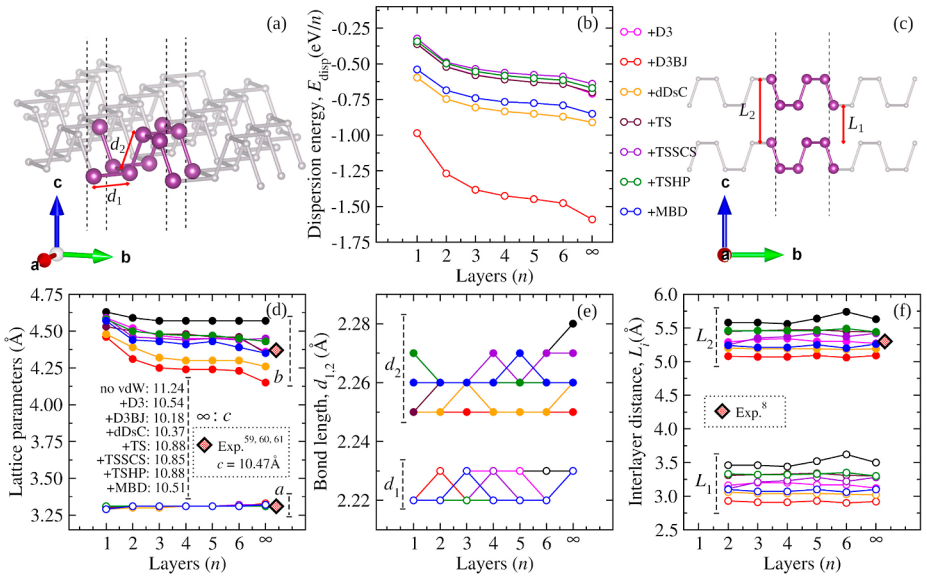

Figure 2. (a) P−P distances marked along both zigzag (d_1) and armchair (d_2) directions. Corresponding quantifications (e) are depicted for all optimizations using vdW corrections. (b) Dispersion energies with respect to the number of layers (n), given by eV/n, for all vdW correction models. (c) Interlayer distances represented for both top-bottom (L_1) and top−top (L_2), and (f) the corresponding average values quantified for n = 1 up to bulk for each vdW model. (d) Lattice parameters for layers and bulk, denoted as a and b vectors, where the numbers listed correspond to the c vector for the bulk (∞). Red diamonds highlight the experimental values for the lattice parameters[59−61] and L_2 interlayer distance,[8] and vdW-color association for the lines is defined as no vdW-black, D3-pink, D3BJ-red, dDsC-orange, TS-brown, TSSCS-violet, TSHP-green, and MBD-blue.

- Scanning Coulomb potential models: use $H(\mathbf{k})$ to scan 2D and 3D Coulomb potential models, denoted as $V(\mathbf{Q})$, to describe exciton e−h interactions within the WanTiBEXOS code (TB-BSE). The models include bare (V3D) and screened (V3DL) for 3D Coulomb potentials, as well as 2D models like those proposed by Keldysh (V2DK),[47] Rytova−Keldysh (V2DRK),[48,49] truncated (V2DT),[50] and its modified version (V2DT2).[51] Detailed descriptions of all models and parameters used, particularly in the 2D $V(\mathbf{Q})$ models, can be found in the Supporting Information. At this stage, we utilized the P_n systems optimized without vdW corrections.
- (W)TB-BSE excitonic properties calculation: employ the defined $V(\mathbf{Q})$ within (W)TB-BSE for all P_n systems obtained from vdW corrections to calculate excitonic properties.

2.1. Total Energy, Geometry Optimization, and vdW Corrections. For the full relaxation of multilayers, we employed the DFT[52,53] semilocal formulation proposed by Perdew, Burke, and Ernzerhof (PBE)[54] for the *xc* energy functional, as implemented in the Vienna Ab initio Simulation Package (VASP).[55,56] In the VASP implementation, we utilized the projector augmented-wave method[57] to solve the KS equations, incorporating a fully relativistic approach to describe the core states. The phosphorus valence electrons were modeled with electron configurations of $3s^2$ and $3p^3$. In the VASP calculations, Brillouin zone integration was performed with a **k**-point mesh of 15 × 11 × **Z**, where **Z** = 3 for n = 1, **Z** = 2 for n = 2 and 3, and **Z** = 1 for n = 4, 5, and 6. For bulk, we set 15 × 11 × 4. These grids were automatically generated through the Monkhorst−Pack protocol. The plane waves were expanded up to a cutoff energy of 500 eV for all 2D systems. The total energy convergence criterion of 10^{-6} eV was employed throughout the calculations.

The Hellmann−Feynman forces were relaxed to values of less than 1 meV/A on every atom. The optimization of forces for phosphorene multilayers included an additional dispersion energy term in the KS total energy. Several E_{disp} treatments were employed, incorporating empirical D3 corrections and its BJ damping function version (D3BJ) proposed by Grimme,[32,34] as well as semiempirical approaches based on dDsC[41,42] and Tkatchenko−Scheffler methods, such as TS, TSHP, TSSCS, and MBD.[36−38]

2.2. Gap Calculation via DFT-1/2. For bandgap energies, excluding excitonic effects, we employed the DFT-1/2 QP correction method,[44] which maintains computational costs at the standard DFT level. DFT-1/2 utilizes the Slater transition technique extended to crystalline systems simulated via DFT,[44,58] where a half-occupation scheme is employed, considering the valence band maximum hybridization for 3sp states in the P atoms (weighted as 0.1 from s and 0.4 from p). The half-occupation is determined through the modified KS potential, defined as $V_{\mathrm{mod},KS} = V_{KS}(\vec{r}) - V_S(\vec{r})$, where $V_{KS}(\vec{r})$ represents the standard KS potential and $V_S(\vec{r})$ is the self-energy potential given by $V_S(\vec{r}) = \Theta(\vec{r}, \mathrm{CUT})[V_{ae}(\vec{r}) - V_{ae-1/2}(\vec{r})]$. The $\Theta(\vec{r}, \mathrm{CUT})$ parameter is a cutoff function determined variationally to prevent an overlap of the Coulomb tails into neighboring atom sites, maximizing the gap energy without considering empirical parameters. Figure S1 in Supporting Information illustrates the good structural transferability (n = 1 → 2 → bulk) of the variationally optimized CUT parameter, which remains at a value of $3.20a_0$, wherein a_0 is the Bohr radius.

2.3. Excitonic Properties Determined Using the Bethe−Salpeter Formalism within TB Calculations. The orthogonal TB Hamiltonian, obtained through the Wannier90 framework, is expressed as follows

$$H(\mathbf{k}) = H_0 + \sum_{i=1}^{N} e^{i\mathbf{k}\cdot\mathbf{R}_i} H_{\mathbf{R}_i} \quad (1)$$

where H_0 represents the matrix elements of the Hamiltonian for the unit cell, incorporating on-site energies and hopping parameters and $H_{\mathbf{R}_i}$ is the hopping matrices describing the interaction between the unit cell and its neighboring cells. The matrices H_0 and $H_{\mathbf{R}_i}$, obtained using the Wannier90 package,[45] were utilized as input for the WanTiBEXOS code[46] to calculate optical properties, incorporating excitonic effects.

The solution of the TB-BSE equation involved solving the exciton Hamiltonian (H_{exc}), defined as

$$H_{exc} = H_e + H_h + V(\mathbf{Q}) \quad (2)$$

where H_e represents the single-particle electron Hamiltonian component, H_h is the hole component, and $V(\mathbf{Q})$ is the Coulomb interaction potential that characterizes the binding of e−h pairs. A comprehensive explanation of the TB-BSE formalism, as implemented in WanTiBEXOS, is provided in the Supporting Information, including details about the Coulomb potential models and the strategies employed for calculating the dielectric constant when necessary.

3. RESULTS

3.1. Structural Analysis. We conducted an analysis of several structural parameters for the P_n systems (n = 1, 2, 3, 4, 5, and 6 as the number of layers) as a slab model with 17 A of vacuum, including ab-plane lattice parameters, average bond lengths (d_1 and d_2), and interlayer distances (for $n > 1$) for top-bottom (L_1) and top−top (L_2), as depicted in Figure 2a,c. Additionally, Figure 2b quantifies the contribution of energy dispersion (E_{disp} in eV/n) from the employed vdW models, both in and intra layers. It is observed that the E_{disp} values exhibit a trend similar to that of n for P_n systems. Specifically, from n = 4 onward, the E_{disp} values remain relatively constant, adding only a small energy portion in the module for the bulk system. Regarding the magnitude of E_{disp}, which plays a crucial role in the structural profile and indirectly affects the calculated optoelectronic properties of P_n, we observe three distinct regions of values among the vdW models: (i) D3BJ imparts the highest dispersion energy contribution, with a difference of approximately 0.61 eV/n for n = 1 → bulk. (ii) dDsC and MBD exhibit similar behavior, and the difference in energy contribution for n = 1 → bulk decreases to around 0.31 eV/n. (iii) D3, TS, TSSCS, and TSHP form a set with the lowest dispersion energy contribution portion. The difference for n = 1 → bulk remains around 0.31 eV/n within this group.

In accordance with the E_{disp} contributions, Figure 2d illustrates the lattice parameters for the n = 1, 2, 3, 4, 5, and 6 layers (a and b vectors) and for the bulk (a, b, and c vectors) for all employed vdW models. Thanks to the attractive performance of the vdW interaction, all models induce a contraction of the b vector (i.e., armchair direction contraction as layers are added) compared to systems without vdW correction, while the a vector (zigzag direction) remains slightly constant for both the vdW model and the number of layers. This behavior is in agreement with results obtained through optB88-vdW functional, in which a = 3.32−3.34 Å and b = 4.58−4.47 Å from monolayer (throughout n = 2, 3, 4, and 5) up to bulk.[18] For the bulk structure, all vdW models promote a contraction of the c vector [as numerically depicted in panel (d)]. Notably, the sequence of shortening follows the same order as the E_{disp} magnitude for the c vector: D3BJ < dDsC < MBD < D3 < TSSCS, TSHP, and TS. By comparing with experimental values for the lattice parameters,[59−61] we found that a vector for zigzag direction fits very well with experiments (a = 3.31 Å) independently of the vdW model employed. However, only D3, dDsC, and MBD models resulted in b for armchair direction and c vectors very close to the experiments (i.e., b = 4.37 Å and c = 10.47 Å).

For stacked layers, our findings suggest that all vdW models have negligible effects on the zigzag direction of P_n multilayers, while they significantly impact the armchair direction, including the layer normal c vector for the bulk. We observed a correlation between the E_{disp} magnitude and the b vector concerning the number of layers, stabilizing at n = 4 when no vdW approach is taken as a reference. The highest contractions in b occur in the sequence D3BJ (0.31 Å), D3, MBD, and dDsC (0.22 Å) for n = 1 → bulk, while for the others, contractions fall within the interval of 0.06−0.15 Å. The P−P distances in the zigzag plane (d_1) and armchair (d_2), quantified in Figure 2e, follow a similar pattern in response to the impact of the vdW models on the a and b lattice vectors. Changes in d_1 are minimal compared to those in d_2 for armchair bonds. Conversely, in alignment with the observation on the c vector for the bulk, interlayer distances, such as top-bottom (L_1) and top−top (L_2) distances, are highly sensitive to the effects of E_{disp} magnitude contribution, given the expected vdW homostructures morphology for n > 1 layers. Thus, the sequence of shortening for L_1 and L_2 correlates with the E_{disp} magnitude, specifically, $L_1(L_2)$: D3BJ < dDsC < MBD < D3 < TSSCS, TSHP, and TS < no vdW. Furthermore, even though all the L_2 values from the vdW model are into 5.1−5.7 Å interval, D3, dDsC, and MBD models (in agreement with the lattice parameter result) are the closest to the 5.3 Å value as the L_2 experimental interlayer distance.[8] This set of structural consequences, ordered by the E_{disp} intensity, impacts the thermodynamic stability and optoelectronic properties of P_n multilayer systems, as discussed in the following sections.

3.2. Stability Analysis. To investigate the thermodynamic stability of the P_n multilayers, we calculated the enthalpy of aggregation (ΔH_{ag}), representing the heat released during the formation of multilayers ($nP_1 \rightarrow P_n$), for all employed vdW models and as a function of the number of layers. Figure 3a illustrates the ΔH_{ag} values for each interface P_n−P_1 formed (i.e., $n - 1$ as the number of interfaces). Throughout the aggregation process from n = 2 to 6, the calculated ΔH_{ag} values for all vdW models indicate an exothermic process. This suggests that the heat released during the inclusion of one monolayer is consistent and independent of the number of layers in the substrate, reflecting the layer−layer interaction in the $P_{(n-1)} + P_1 \rightarrow P_n$ aggregation process. Additionally, the magnitude of the released heat roughly follows the sequence of E_{disp} magnitude observed in the structural discussion. D3BJ exhibits the highest exothermic aggregation process, while the no vdW calculations show the lowest, with a difference of around 450 meV/($n - 1$). The ΔH_{ag} values for other vdW models lie between −300 and −400 meV/($n - 1$).

As structural distortion is expected with the addition of a new monolayer in the P_n system, we calculated the enthalpy portion related to distortion (ΔH_{dis}) to investigate the associated heat contribution. Figure 3b presents the average ΔH_{dis} for the multilayer systems, along with their standard deviation indicated by the vertical bars, in relation to the P_1 pristine monolayer, as described by the equation. It is evident

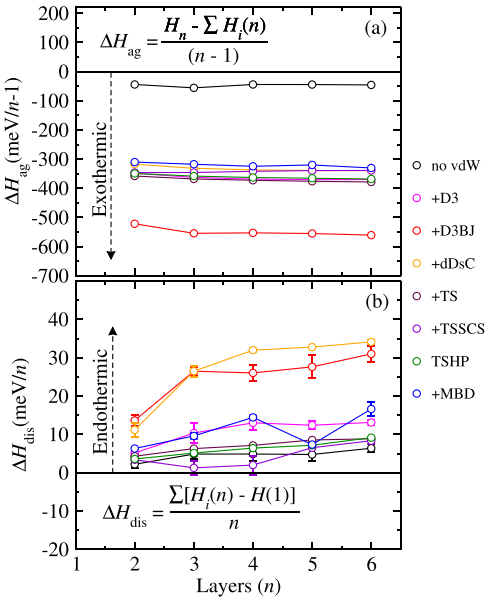

Figure 3. (a) Enthalpy of aggregation (ΔH_{ag} in meV) with respect to the number of interfaces ($n - 1$), as indicated by the equation shown in the figure in which H_n is the enthalpy of the layered systems and $H_i(n)$ is the enthalpy of the individual layers as part of a given n. Decrease in these values toward negative numbers signifies the exothermic energy released during the aggregation process of n layers. (b) Average enthalpy of distortion (ΔH_{dis} in meV) for each layer along with the standard deviation (represented by vertical bars). These values are associated with the heat involved in the distortion contribution of individual layers with respect to the P_1 pristine monolayer, i.e., $H(1)$.

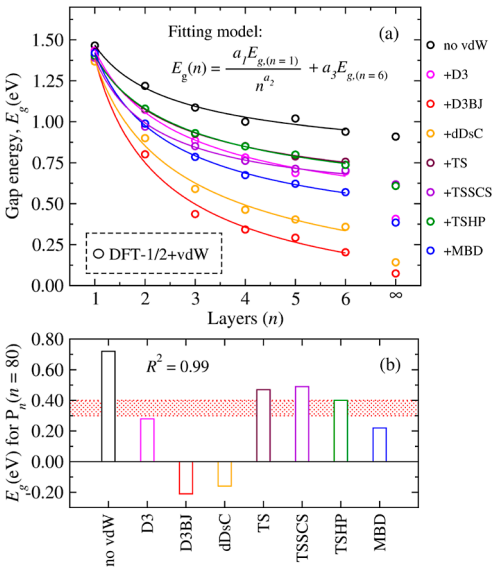

Figure 4. (a) Gap energy (E_g) calculated without excitonic effects via DFT-1/2 for P_n and bulk optimized using all vdW correction models. Solid lines represent the decreasing trend from $n = 1 \rightarrow 6$, based on the indicated model and optimized a, b, and c parameters. (b) E_g for P_{80} (reaching the bulk gap value)[17,62] calculated through the fitting model derived from all vdW correction models. Red shaded region represents the experimental gap interval of E_g = 0.3−0.4 eV reported through PL[63] and scanning tunneling[64] spectroscopy experiments.

that the aggregation of monolayers ($nP_1 \rightarrow P_n$) induces a distortion process in each monolayer, contributing heat in an endothermic manner. In line with the E_{disp} contributions influencing structural parameters, such as contractions of the b vector, $L_1(L_2)$ interlayer distances, and a higher dispersion of the d_2 bond length values, D3BJ and dDsC resulted in the highest ΔH_{dis} values, as expected.

3.3. Gap Energy via DFT-1/2+vdW. To employ an economical and effective method for bandgap correction, DFT-1/2 was utilized with the optimization of the CUT parameter for both P_1 and P_2 systems (Figure S1). The consistent CUT = $3.20a_0$ for both systems indicates the method's good transferability. Based on this, Figure 4a illustrates the bandgap values (E_g) for P_n multilayers obtained through DFT-1/2 (without excitonic effects) for all vdW methods using the optimized CUT parameter. The DFT-1/2+vdW, based on the PBE functional, significantly improves the E_g values compared to plain PBE + vdW, while keeping the computational cost at the level of standard DFT based on the PBE xc functional (as depicted in Table S1 in Supporting Information). Thus, our proposed bandgap calculation protocol without excitonic effects serves as a preliminary step for obtaining excitonic properties through the wannierization process, subsequently employing the TB-BSE protocol.

First, a strong dependence of E_g on the number of layers from n = 1 up to 6 and the bulk is observed, reflecting an exponential decay relation indicative of thickness dependence and quantum confinement effects. This trend aligns with findings from previous experimental and theoretical studies.[43,63,65−67] For n = 1, DFT-1/2 provides E_g values in the 1.37−1.47 eV range for all vdW models. These values exhibit the lowest set of deviations ($|\Delta E_g| < 5\%$) compared to the 1.45 eV obtained via PL,[14−16] as illustrated in Figure 4b. In this context, our DFT-1/2 protocol (based on PBE) at the standard DFT level demonstrates good agreement with computationally expensive HSE06 + vdW (1.51 eV) and mBJ + vdW (1.41 eV) xc functionals.[18]

For n = 2, 3, 4, 5, 6, and bulk, our findings demonstrate that the DFT-1/2 bandgap magnitude strongly depends on the employed vdW approximation. However, the trend maintains a large gap for the monolayer, gradually decreasing to narrower bandgaps for the bulk. Specifically, D3, D3BJ, dDsC, TSSCS, and MBD yielded E_g values lower than those obtained via PL in the n = 2−5 range, with $|\Delta E_g| < 30\%$ (with TS presenting the lowest deviation below 20%). On the contrary, no vdW calculations yielded higher E_g values (except for n = 2).[15,63,66,67] Our results unveil a strong correlation between structural parameters (such as stretching b and $L_{1,2}$ interlayer distance contraction) and E_g. The wave function overlap[18] between different layers is indirectly influenced by the E_{disp} magnitude; for instance, D3BJ maximizes E_{disp}, resulting in the narrowest E_g values.

For the bulk explicitly calculated, the inclusion of vdW corrections leads to a striking scenario, with E_g decreasing to values below 0.11 eV (observed in no vdW and no QP correction, see Table S1). This trend is expected as a consequence of the E_g underestimation inherent to semilocal xc functionals, which falls within 0.04−0.08 eV for plain DFT + vdW calculations. In contrast, DFT-1/2+vdW yields E_g values in the range of 0.08−0.90 eV. The narrowest E_g value is observed for the D3BJ method, aligning with the highest wave function overlap interpretation. This method provides the strongest dispersion energy, resulting in the shortest b parameter and $L_{1,2}$ interlayer distances, thereby maximizing the

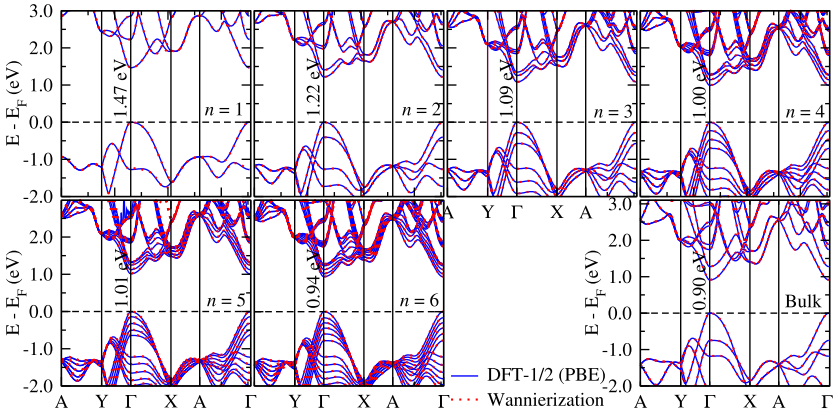

Figure 5. Comparison between DFT-1/2 (blue curves) and wannierization (red dots) band structures (A−Y−Γ−X−A−Γ) for systems with n = 1, 2, 3, 4, 5, and 6 layers and bulk system geometrically optimized without vdW correction (i.e., plain DFT). Valence band maximum (VBM) is set at the Fermi level (0 eV), and the corresponding E_g values obtained through DFT-1/2 are indicated.

wave function overlap. However, this leads to a considerable deviation from experimental results based on PL.[63]

Additionally, based on several fitting functions reported on theoretical and experimental studies on the literature,[14,19,68,69] we employed a fitting model based on $E_g(n) \propto 1/n^a$ (a is an optimized parameter) with our set of DFT-1/2+vdW gap energy results for P_n systems throughout the $n = 1 \rightarrow 6$ interval, since those systems were calculated with $V(\mathbf{Q})$ = V2DRK; all the optimized parameters for the fitting model are depicted in Table S2 (Supporting Information). Since E_g reaches the bulk value for P_{80},[17,62] Figure 4b shows the $E_g(n)$ estimated from n = 80 through our fitting model, and the numerical data are available in Table S2. D3 and MBD models presented concurrent agreement with DFT-1/2+vdW calculations and experiments (red shaded region) based on PL[63] and scanning tunneling[64] spectroscopy.

The DFT-1/2+vdW results reveal a high sensitivity of the gap energy in P_n layers and the bulk concerning the employed vdW method. While all protocols summarize the gap energy dependence on thickness, one must be mindful of the indirect effects of empirical and semiempirical vdW methods on gap energies due to their impact on the structure, even when working at the same level of theory. Conversely, our protocol, combining DFT + vdW with QP correction, stands as a compelling option for initiating investigations into excitonic effects, offering more accurate gap energy values within a cost-effective computational framework.

3.4. Wannierization and Exciton Calculations. Our investigation of excitonic effects in P_n is based on constructing the MLWF Hamiltonian. We utilized the MLWF-TB protocol to incorporate the Hamiltonian into the (W)TB + BSE formalism, allowing us to obtain optical properties with excitonic effects. Beginning with no vdW calculations, we derived the scissors operator (SCS) from our TB Hamiltonian. This was constructed through the MLWF-TB parametrization (s and p orbitals of P atoms) over the DFT-1/2 band structures, as illustrated in Figure 5. In this figure, all DFT-1/2 band gap values are indicated, showcasing a perfect fit of electronic bands around and away from the Fermi level (E_F) along the A−Y−Γ−X−A−Γ path for P_n systems with n = 1, 2, 3, 4, 5, 6 layers, as well as bulk; Figure S2 provides a full k-path for the bulk by involving the k_z direction. The bandgap is approximately located at the Γ-point, indicating a very flat band dispersion along the Γ → X (zigzag) direction. This suggests that charge carriers are confined in the effective 1D environment along the armchair direction (Γ → Y).[70]

For the (W)TB + BSE approach, we conducted convergence studies and screened the ground-state exciton binding energy (E_b). This parameter is defined as the difference between the direct bandgap, $E_g^{\text{DFT-1/2}}$, and the excitonic ground state, $E_{\text{opt}}^{\text{TB}}$. We explored various Coulomb potentials for the e−h pairwise interactions [$V(\mathbf{Q})$ = V3D, V3DL, V2DK, V2DRK, V2DT, and V2DT2] for the P_n systems optimized without the vdW method. It is noteworthy that $E_g^{\text{DFT-1/2}}$ and E_g^{TB} (as the DFT and TB electronic gap energies) are coincident, justifying the procedure of calculating $E_b = E_g^{\text{DFT-1/2}} - E_{\text{opt}}^{\text{TB}}$, where $E_{\text{opt}}^{\text{TB}}$ is the optical band gap obtained via (W)TB-BSE. Detailed optical (and QP) bandgaps under different **k**-mesh densities and E_b values for all $V(\mathbf{Q})$ models can be found in Tables S3 and S4 in Supporting Information. We compared our results with PR−PL[16] and QP-GW calculations[43] from the literature. Among the various Coulomb potentials, we found that $V(\mathbf{Q})$ = V2DRK yielded the best comparative values of E_b, with 0.93 eV for the monolayer (n = 1). This result aligns well with the 0.9 ± 0.1 eV obtained via PR−PL (see Table S4). Consequently, we employed the V2DRK Coulomb potential for all P_n systems optimized in our set of vdW methods, given the good transferability of these potentials. For the bulk, a comparison between V3D and V3DL potentials revealed that the first is the suitable one since its topology requires periodicity throughout all dimensions.

Figure 6 illustrates the ground-state E_b calculated by using the V2DRK Coulomb potential for e−h pairwise interactions within the (W)TB-BSE protocol for all P_n systems, considering various vdW methods. For n = 1, our results are consistent with experimental data from PR−PL,[16] in contrast to the significantly underestimated and computationally intensive QP-GW calculations.[43] As for n > 1, E_b values were fitted for each vdW model using the same shape of equation employed for $E_g^{\text{DFT-1/2}}$ in Figure 5; the b_1, b_2, and b_3 fitting parameters are depicted in Table S5 in Supporting Information, from which all the functions yield R^2 = 0.99. It is evident that E_b exponentially decreases in accordance with the reduction in quantum confinement resulting from the additional stacking layers, providing evidence of wave function overlap in the P_{n+1} systems. The E_b values for the layers align with the magnitude of the E_{disp} energies, consistent with their impact on $E_g^{\text{DFT-1/2}}$ values. For instance, D3BJ yields the lowest set of E_b values for

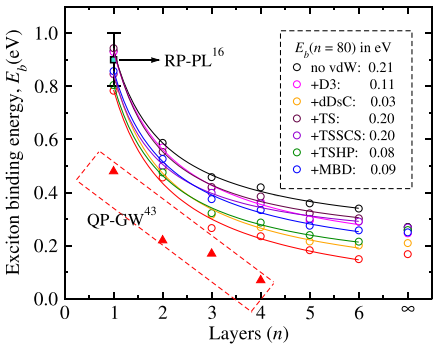

Figure 6. Exciton binding energy (E_b) calculated using the $V(\mathbf{Q})$ = V2DRK Coulomb potential for electron−hole pairs within the (W)TB-BSE approach for all P_n layered systems, whereas for the bulk, the $V(\mathbf{Q})$ = V3D was employed, taking each structure optimized using various vdW methods. PR−LP experiments[16] reporting a monolayer $E_b = 0.9 \pm 0.1$ eV and the underestimation of theoretical calculations based on the QP-GW approach[43] are indicated. While $n = \infty$ correspond to the E_b explicitly calculated for the bulk, the highlighted numbers show the E_b values for $n = 80$ based on the fitting model by employing the range $n = 1 \rightarrow 6$.

the exciton ground state, while no vdW protocol provides the highest set of values.

By utilizing the fitting function applied to the E_b values across the range $n = 1 \rightarrow 6$, we extrapolated the correspondence between the bulk and the E_b values attained at $n = 80$ for all vdW models. This procedure is similar to that one employed for the band gap, which permits us to verify the matching between $E_g(n = 80)$ and $E_b(n = 80)$ through the fitting models. The highlighted numbers in Figure 6 reveal that D3, TS, TSSCS, TSHP, and MBD are the vdW methods for which the bulk E_b value aligns with the fitting, consistent with their effective calculations, such as E_b for $n = \infty$. Conversely, D3BJ presented a spurious result with a negative $E_b = -0.04$ eV, which is a consequence of the great underestimation of the band gap. Consequently, considering all the protocols employed—initiating with the relativistic treatment of the bandgap at the DFT level and progressing to the TB-BSE approach for excitonic calculations—we conclude that the D3 and MBD vdW corrections exhibit notable performance in describing the indirect effects of the structural profile on the optoelectronic properties of multilayer BP systems.

Given that the MBD provides one of the best performances for the set of electronic and structural properties in agreement with the experiment, as observed in Figure 2d,f, we advance to the optoelectronic properties of P_n systems by aiming for a better understanding of the BP stacking and the impact of MBD vdW correction, which is depicted in Figure 7 for the exciton absorption spectrum (BSE) through the light polarizations along the x direction (α_x) and y direction (α_y). A comparison is made for all P_n systems from $n = 2$ to bulk with particular emphasis on the monolayer. The vertical lines in the spectra represent the single-particle gap energies (E_g) obtained through DFT-1/2. In our results for $\alpha_{x,y}$, the previously observed orthogonality between heat and electron transport in monolayer BP is extended to systems with a few layers up to the bulk. This orthogonality effect, reported in previous studies,[71] continues to influence the optical properties in multilayer systems. As a consequence of the wave function overlap in P_{n+1} systems, a significant in-plane anisotropy is observed when comparing α_x and α_y. For $n > 1$, the α_x spectra are notably suppressed, indicating the presence of collective electronic excitations below E_g values, especially relative to the armchair (y) direction. This result reinforces the impact of linear polarization direction on the incident light, demonstrating that even with just a few stacked layers, BP's optoelectronic properties can be finely tuned.

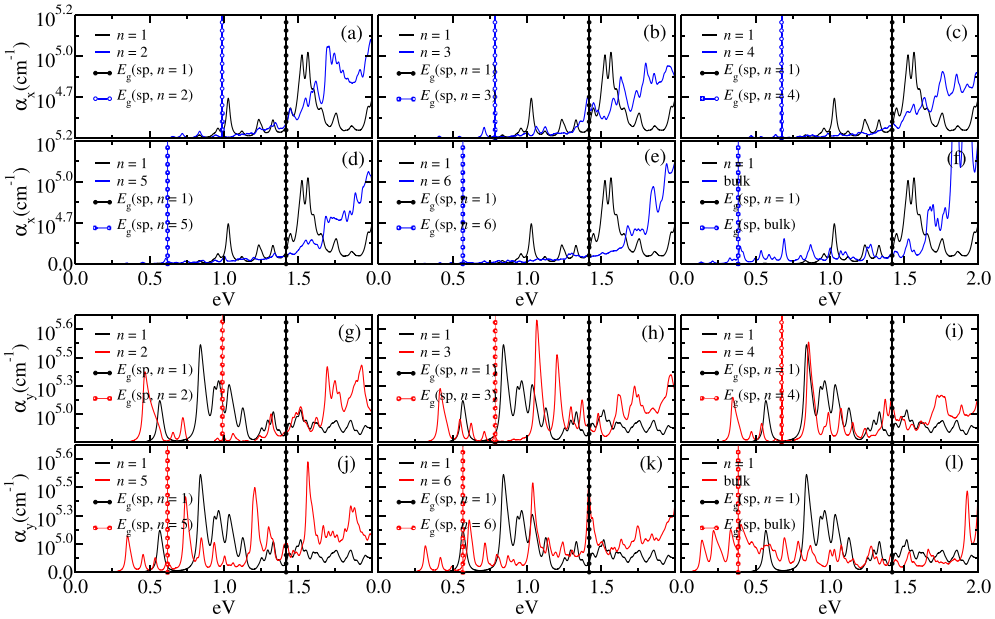

Figure 7. Absorption coefficients (α) calculated for light polarizations along the x direction (α_x) and y direction (α_y). For P_n layered systems with various numbers of layers (n = 1, 2, 3, 4, 5, and 6) and bulk, all geometrically optimized with MBD vdW correction, so that $V(\mathbf{Q})$ = V2DRK Coulomb potential was used for the layers, and for the bulk, the $V(\mathbf{Q})$ = V3D was employed. Panels (a−f) show α_x, while panels (g−l) depict α_y. Plot organization facilitates the comparison between systems with more than one layer ($n > 1$) and the monolayer ($n = 1$), emphasizing their respective single-particle (E_g) values obtained through DFT-1/2.

4. SUMMARY

We conducted a comprehensive and systematic investigation at various theoretical levels for BP systems spanning from monolayer (n = 1) to bulk, including n = 2, 3, 4, 5, and 6 layers, with structural optimizations performed using different empirical (D 3 and D 3BJ) and semiempirical (dD sC, TS, TSHP, TSSCS, and MBD) vdW methods to enhance interlayer nonbonded interactions. The characterization of optoelectronic properties involved a combination of protocols, starting with bandgap corrections using relativistic QP correction (DFT-1/2). The resulting corrected band structures were then used to construct a TB Hamiltonian through a MLWF-TB approach, followed by the solution of the BSE in the TB framework. Our D FT-1/2+vdW approach revealed a high sensitivity of the gap energy in P_n layers and bulk to the choice of vdW methods. This emphasizes the need for careful consideration when employing empirical and semiempirical vdW methods to minimize significant underestimations of gap energies by enhancing interlayer wave function overlap. Additionally, our semiempirical approach for calculating excitonic properties, particularly the screening of e−h interactions based on TB 2D and 3D Coulomb potential models, requires attention. The Rytova−Keldysh potential proved to be effective i n d escribing t he t ransition f rom the monolayer to bulk, providing exciton binding energies that were in excellent agreement with PL results from the literature, unlike the more computationally expensive QP-GW alternatives. Furthermore, our fitting m odel, a pplied t o both bandgap and exciton binding energy results, demonstrates that in particular for phosphorene, the performance of the D3 and MBD method was coherent with experiments based on monolayer and bulk, in order that its application for a 2D system with different c hemical c omposition a nd topology needs some care. On the other hand, our result provides a particular evidence based on the achieving equivalence between bulk calculations and the values obtained for n = 80 layers, indicating the reliability of D3 and MBD throughout the stacking of phosphorene layered.

ASSOCIATED CONTENT

Data Availability Statement

All the DFT calculations were carried out using VASP 5.4.4 (https://www.vasp.at/). The creation of conformers for the scan calculations was generated using the open-source PyMOL Application Programming Interface (API) (https://github.com/schrodinger/pymol-opensource). The bandgap correction performed to all the systems based in all vdW correction was based on QP relativistic correction DFT-1/2 (https://github.com/Celso0408/DFT-1-2). The maximally localized Wannier functions to orthogonal TB Hamiltonian—$H(\mathbf{k})$—were obtained through Wannier90 (https://wannier.org/), in which a proper set of parameters was used (https://github.com/dguedessob/phosphorene_wannier90.git). Thus, $H(\mathbf{k})$ was used as inputs into WanTiBEXOS to resolutions of the BSE (https://github.com/dguedessob/wantibexos_phosphorene.git), which were performed through the WantiBEXOS code (https://wantibexos.readthedocs.io/en/latest/ and https://github.com/ac-dias/wantibexos). Visualization and pictures were made using Visualization for Electronic and Structural Analysis (VESTA, https://jp-minerals.org/vesta/en/).

AUTHOR INFORMATION

Corresponding Authors

Diego Guedes-Sobrinho − *Chemistry Department, Federal University of Paraná, Curitiba 81531-980, Brazil;* orcid.org/0000-0002-3313-2822; Email: guedessobrinho@ufpr.br

Celso R. Caldeira Rêgo − *Institute of Nanotechnology, Karlsruhe Institute of Technology (KIT), Eggenstein-Leopoldshafen 76344, Germany;* orcid.org/0000-0003-1861-2438; Email: celso.rego@kit.edu

Maurício J. Piotrowski − *Department of Physics, Federal University of Pelotas, Pelotas, Rio Grande do Sul 96010-900, Brazil;* orcid.org/0000-0003-3477-4437; Email: mauriciomjp@gmail.com

Alexandre Cavalheiro Dias − *Institute of Physics and International Center of Physics, University of Brasília, Brasília 70910900, Brazil;* orcid.org/0000-0001-5934-8528; Email: alexandre.dias@unb.br

Authors

Gabriel Reynald Da Silva − *Chemistry Department, Federal University of Paraná, Curitiba 81531-980, Brazil*

Henrique R. Da Silva − *Chemistry Department, Federal University of Paraná, Curitiba 81531-980, Brazil*

W. Wenzel − *Institute of Nanotechnology, Karlsruhe Institute of Technology (KIT), Eggenstein-Leopoldshafen 76344, Germany;* orcid.org/0000-0001-9487-4689

Notes

The authors declare no competing financial interest.

ACKNOWLEDGMENTS

The authors are thankful for the financial support provided by the National Council for Scientific and Technological Development (CNPq, grant nos. 307345/2021-1, 408144/2022-0, and 305174/2023-1), the Federal District Research Support Foundation (FAPDF, grant nos. 00193-00001817/2023-43 and 00193-00001817/2023-43), the Coordination for Improvement of Higher Level Education (CAPES), the Rio Grande do Sul Research Foundation (FAPERGS), and the German Federal Ministry of Education and Research (BMBF) for funding the Innovation-Platform MaterialDigital (www.materialdigital.de) project under project no. FKZ 13XP5094A. The authors acknowledge the use of the HoreKa supercomputer, supported by the Ministry of Science, Research and the Arts Baden-Württemberg and the Federal Ministry of Education and Research. Additionally, the authors extend their thanks to the "Centro Nacional de Processamento de Alto Desempenho em São Paulo" (CENAPAD-SP, UNICAMP/FINEP—MCTI project) for providing resources for projects 897 and 570, to Lobo Carneiro HPC (NACAD) at the Federal University of Rio de Janeiro (UFRJ) for resources for project 133, to CIMATEC SENAI at Salvador—BA, Brazil, for their partnership and support through the Ogun Supercomputer,

and to the "Laboratório Central de Processamento de Alto Desempenho" (LCPAD) financed by FINEP through CT-INFRA/UFPR projects.

REFERENCES

(1) Li, L.; Yu, Y.; Ye, G. J.; Ge, Q.; Ou, X.; Wu, H.; Feng, D.; Chen, X. H.; Zhang, Y. Black Phosphorus Field-Effect Transistors. *Nat. Nanotechnol.* **2014**, *9*, 372−377.

(2) He, G.; Dong, T.; Yang, Z.; Ohlckers, P. Tuning 2D Black Phosphorus: Defect Tailoring and Surface Functionalization. *Chem. Mater.* **2019**, *31*, 9917−9938.

(3) Yan, W.; Shresha, V. R.; Jeangros, Q.; Azar, N. S.; Balendhran, S.; Ballif, C.; Crozier, K.; Bullock, J. Spectrally Selective Mid-Wave Infrared Detection Using Fabry-Pérot Cavity Enhanced Black Phosphorus 2D Photodiodes. *ACS Nano* **2020**, *14*, 13645−13651.

(4) Seiler, H.; Zahn, D.; Zacharias, M.; Hildebrandt, P.-N.; Vasileiadis, T.; Windsor, Y. W.; Qi, Y.; Carbogno, C.; Draxl, C.; Ernstorfer, R.; et al. Accessing the Anisotropic Nonthermal Phonon Populations in Black Phosphorus. *Nano Lett.* **2021**, *21*, 6171−6178.

(5) Han, D.; Han, X.; Liu, L.; Li, D.; Liu, Y.; Liu, Z.; Liu, D.; Chen, Y.; Zhuo, K.; Sang, S. Sub-ppb-Level Detection of Nitrogen Dioxide Based on High-Quality Black Phosphorus. *ACS Appl. Mater. Interfaces* **2022**, *14*, 13942−13951.

(6) Du, K.; Lv, Q.; Liang, Z.; Liu, G.; Hussain, S.; Liu, J.; Qiao, G. Trends in the Preparation and Passivation Techniques of Black Phosphorus Nanostructures for Optoelectronics Applications: A Review. *ACS Appl. Nano Mater.* **2023**, *6*, 3159−3183.

(7) Buscema, M.; Groenendijk, D. J.; Blanter, S. I.; Steele, G. A.; van der Zant, H. S. J.; Castellanos-Gomez, A. Fast and Broadband Photoresponse of Few-Layer Black Phosphorus Field-Effect Transistors. *Nano Lett.* **2014**, *14*, 3347−3352.

(8) Xia, F.; Wang, H.; Jia, Y. Rediscovering Black Phosphorus as an Anisotropic Layered Material for Optoelectronics and Electronics. *Nat. Commun.* **2014**, *5*, 4458.

(9) Wei, Q.; Peng, X. Superior mechanical flexibility of phosphorene and few-layer black phosphorus. *Appl. Phys. Lett.* **2014**, *104*, 251915.

(10) Castellanos-Gomez, A. Black Phosphorus: Narrow Gap, Wide Applications. *J. Phys. Chem. Lett.* **2015**, *6*, 4280−4291.

(11) Su, B.-W.; Li, X.-K.; Jiang, X.-Q.; Xin, W.; Huang, K.-X.; Li, D.-K.; Guo, H.-W.; Liu, Z.-B.; Tian, J.-G. Carrier Engineering in Polarization-Sensitive Black Phosphorus van der Waals Junctions. *ACS Appl. Mater. Interfaces* **2018**, *10*, 35615−35622.

(12) Xia, F.; Wang, H.; Hwang, J. C. M.; Neto, A. H. C.; Yang, L. Black Phosphorus and its Isoelectronic Materials. *Nat. Rev. Phys.* **2019**, *1*, 306−317.

(13) Dong, B.; Huang, L.; Lee, C.; Ang, K.-W. Black Phosphorus Based Photodetectors. In *Fundamentals and Applications of Phosphorus Nanomaterials*; American Chemical Society, 2019; pp 135−153. Chapter 7.

(14) Yang, J.; Xu, R.; Pei, J.; Myint, Y. W.; Wang, F.; Wang, Z.; Zhang, S.; Yu, Z.; Lu, Y. Optical Tuning of Exciton and Trion Emissions in Monolayer Phosphorene. *Light Sci. Appl.* **2015**, *4*, No. e312.

(15) Liu, H.; Neal, A. T.; Zhu, Z.; Luo, Z.; Xu, X.; Tománek, D.; Ye, P. D. Phosphorene: An Unexplored 2D Semiconductor with a High Hole Mobility. *ACS Nano* **2014**, *8*, 4033−4041.

(16) Wang, X.; Jones, A. M.; Seyler, K. L.; Tran, V.; Jia, Y.; Zhao, H.; Wang, H.; Yang, L.; Xu, X.; Xia, F. Highly Anisotropic and Robust Excitons in Monolayer Black Phosphorus. *Nat. Nanotechnol.* **2015**, *10*, 517−521.

(17) Chen, C.; Chen, F.; Chen, X.; Deng, B.; Eng, B.; Jung, D.; Guo, Q.; Yuan, S.; Watanabe, K.; Taniguchi, T.; et al. Bright Mid-Infrared Photoluminescence from Thin-Film Black Phosphorus. *Nano Lett.* **2019**, *19*, 1488−1493.

(18) Qiao, J.; Kong, X.; Hu, Z.-X.; Yang, F.; Ji, W. High-Mobility Transport Anisotropy and Linear Dichroism in Few-Layer Black Phosphorus. *Nat. Commun.* **2014**, *5*, 4475.

(19) Zhang, G.; Chaves, A.; Huang, S.; Wang, F.; Xing, Q.; Low, T.; Yan, H. Determination of Layer-Dependent Exciton Binding Energies in Few-Layer Black Phosphorus. *Sci. Adv.* **2018**, *4*, No. eaap9977.

(20) Wei, Y.; Jiang, Y.; Pang, K.; Xu, X.; Kaner, N. T.; Li, X.; Yang, J.; Zhang, G.; Li, W.; Jiang, Y.; et al. Long Radiation Lifetime and Quasi-Isotropic Excitons in Antioxidant V−V Binary Phosphorene Allotropes with Intrinsic Dipole. *J. Phys. Chem. C* **2020**, *124*, 14787−14796.

(21) Pham, P. V.; Bodepudi, S. C.; Shehzad, K.; Liu, Y.; Xu, Y.; Yu, B.; Duan, X. 2D Heterostructures for Ubiquitous Electronics and Optoelectronics: Principles, Opportunities, and Challenges. *Chem. Rev.* **2022**, *122*, 6514−6613.

(22) Eslamibidgoli, M. J.; Eikerling, M. H. Mechanical and Chemical Stability of Monolayer Black Phosphorous Studied by Density Functional Theory Simulations. *J. Phys. Chem. C* **2018**, *122*, 22366−22373.

(23) Peng, Y.; Lu, B.; Wang, N.; Lu, J. E.; Li, C.; Ping, Y.; Chen, S. Oxygen Reduction Reaction Catalyzed by Black-Phosphorus-Supported Metal Nanoparticles: Impacts of Interfacial Charge Transfer. *ACS Appl. Mater. Interfaces* **2019**, *11*, 24707−24714.

(24) Barik, G.; Pal, S. Energy Gap-Modulated Blue Phosphorene as Flexible Anodes for Lithium- and Sodium-Ion Batteries. *J. Phys. Chem. C* **2019**, *123*, 2808−2819.

(25) Wang, Z.; Lv, P.; Becton, M.; Hong, J.; Zhang, L.; Chen, X. Mechanically Tunable Near-Field Radiative Heat Transfer between Monolayer Black Phosphorus Sheets. *Langmuir* **2020**, *36*, 12038−12044.

(26) Gómez-Pérez, J. F.; Correa, J. D.; Pravda, C. B.; Kónya, Z.; Kukovecz, A. Dangling-to-Interstitial Oxygen Transition and Its Modifications of the Electronic Structure in Few-Layer Phosphorene. *J. Phys. Chem. C* **2020**, *124*, 24066−24072.

(27) Cohen, A. J.; Mori-Sánchez, P.; Yang, W. Fractional Charge Perspective on the Band Gap in Density-Functional Theory. *Phys. Rev. B* **2008**, *77*, 115123.

(28) Crowley, J. M.; Tahir-Kheli, J.; Goddard, W. A. Resolution of the Band Gap Prediction Problem for Materials Design. *J. Phys. Chem. Lett.* **2016**, *7*, 1198−1203.

(29) Dion, M.; Rydberg, H.; Schröder, E.; Langreth, D. C.; Lundqvist, B. I. Van Der Waals Density Functional for General Geometries. *Phys. Rev. Lett.* **2004**, *92*, 246401.

(30) Klimeš, J.; Michaelides, A. Perspective: Advances and Challenges in Treating van der Waals Dispersion Forces in Density Functional Theory. *J. Chem. Phys.* **2012**, *137*, 120901.

(31) Grimme, S. Accurate Description of van der Waals Complexes by Density Functional Theory Including Empirical Corrections. *J. Comput. Chem.* **2004**, *25*, 1463−1473.

(32) Grimme, S. Semiempirical GGA-Type Density Functional Constructed with a Long-range Dispersion Correction. *J. Comput. Chem.* **2006**, *27*, 1787−1799.

(33) Grimme, S.; Hansen, A.; Brandenburg, J. G.; Bannwarth, C. Dispersion-Corrected Mean-Field Electronic Structure Methods. *Chem. Rev.* **2016**, *116*, 5105−5154.

(34) Grimme, S.; Antony, J.; Ehrlich, S.; Krieg, H. A Consistent and Accurate Ab Initio Parametrization of Density Functional Dispersion Correction (DFT-D) for the 94 Elements H-Pu. *J. Chem. Phys.* **2010**, *132*, 154104.

(35) Grimme, S.; Ehrlich, S.; Goerigk, L. Effect of the Damping Function in Dispersion Corrected Density Functional Theory. *J. Comput. Chem.* **2011**, *32*, 1456−1465.

(36) Tkatchenko, A.; Scheffler, M. Accurate Molecular Van Der Waals Interactions from Ground-State Electron Density and Free-Atom Reference Data. *Phys. Rev. Lett.* **2009**, *102*, 073005.

(37) Tkatchenko, A.; DiStasio, R. A.; Car, R.; Scheffler, M. Accurate and Efficient Method for Many-Body van der Waals Interactions. *Phys. Rev. Lett.* **2012**, *108*, 236402.

(38) Ambrosetti, A.; Reilly, A. M.; DiStasio, R. A.; Tkatchenko, A. Long-Range Correlation Energy Calculated from Coupled Atomic Response Functions. *J. Chem. Phys.* **2014**, *140*, 18A508.

(39) Bučko, T.; Lebègue, S.; Hafner, J.; Ángyán, J. G. Improved Density Dependent Correction for the Description of London Dispersion Forces. *J. Chem. Theory Comput.* **2013**, *9*, 4293−4299.
(40) Bucko, T.; Lebègue, S.; Ángyán, J. G.; Hafner, J. Extending the applicability of the Tkatchenko-Scheffler dispersion correction via iterative Hirshfeld partitioning. *J. Chem. Phys.* **2014**, *141*, 034114.
(41) Steinmann, S. N.; Corminboeuf, C. Comprehensive Benchmarking of a Density-Dependent Dispersion Correction. *J. Chem. Theory Comput.* **2011**, *7*, 3567−3577.
(42) Steinmann, S. N.; Corminboeuf, C. A Generalized-Gradient Approximation Exchange Hole Model for Dispersion Coefficients. *J. Chem. Phys.* **2011**, *134*, 044117.
(43) Qiu, D. Y.; da Jornada, F. H.; Louie, S. G. Environmental Screening Effects in 2D Materials: Renormalization of the Bandgap, Electronic Structure, and Optical Spectra of Few-Layer Black Phosphorus. *Nano Lett.* **2017**, *17*, 4706−4712.
(44) Ferreira, L. G.; Marques, M.; Teles, L. K. Approximation to Density Functional Theory for the Calculation of Band Gaps of Semiconductors. *Phys. Rev. B* **2008**, *78*, 125116.
(45) Mostofi, A. A.; Yates, J. R.; Lee, Y.-S.; Souza, I.; Vanderbilt, D.; Marzari, N. wannier90: A Tool for Obtaining Maximally-Localised Wannier Functions. *Comput. Phys. Commun.* **2008**, *178*, 685−699.
(46) Dias, A. C.; Silveira, J. F. R. V.; Qu, F. WanTiBEXOS: A Wannier Based Tight Binding Code for Electronic Band Structure, Excitonic and Optoelectronic Properties of Solids. *Comput. Phys. Commun.* **2023**, *285*, 108636.
(47) Dias, A. C.; Bragança, H.; Zeng, H.; Fonseca, A. L. A.; Liu, D.-S.; Qu, F. Large Room-Temperature Valley Polarization by Valley-Selective Switching of Exciton Ground State. *Phys. Rev. B* **2020**, *101*, 085406.
(48) Chaves, A.; Sousa, G. O.; Khaliji, K.; da Costa, D. R.; Farias, G. A.; Low, T. Signatures of Subband Excitons in Few-Layer Black Phosphorus. *Phys. Rev. B* **2021**, *103*, 165428.
(49) Van Tuan, D.; Yang, M.; Dery, H. Coulomb Interaction in Monolayer Transition-Metal Dichalcogenides. *Phys. Rev. B* **2018**, *98*, 125308.
(50) Rozzi, C. A.; Varsano, D.; Marini, A.; Gross, E. K. U.; Rubio, A. Exact Coulomb Cutoff Technique for Supercell Calculations. *Phys. Rev. B* **2006**, *73*, 205119.
(51) Ismail-Beigi, S. Truncation of Periodic Image Interactions for Confined Systems. *Phys. Rev. B* **2006**, *73*, 233103.
(52) Hohenberg, P.; Kohn, W. Inhomogeneous Electron Gas. *Phys. Rev.* **1964**, *136*, B864−B871.
(53) Kohn, W.; Sham, L. J. Self-Consistent Equations Including Exchange and Correlation Effects. *Phys. Rev.* **1965**, *140*, A1133−A1138.
(54) Perdew, J. P.; Burke, K.; Ernzerhof, M. Generalized Gradient Approximation Made Simple. *Phys. Rev. Lett.* **1996**, *77*, 3865−3868.
(55) Kresse, G.; Hafner, J. Ab Initio Molecular Dynamics for Open-Shell Transition Metals. *Phys. Rev. B* **1993**, *48*, 13115−13118.
(56) Kresse, G.; Furthmüller, J. Efficient Iterative Schemes for Ab Initio Total-Energy Calculations Using a Plane-Wave Basis Set. *Phys. Rev. B* **1996**, *54*, 11169−11186.
(57) Blöchl, P. E. Projector Augmented-Wave Method. *Phys. Rev. B* **1994**, *50*, 17953−17979.
(58) Slater, J. C.; Johnson, K. H. Self-Consistent-Field X−α Cluster Method for Polyatomic Molecules and Solids. *Phys. Rev. B* **1972**, *5*, 844−853.
(59) Brown, A.; Rundqvist, S. Refinement of the Crystal Structure of Black Phosphorus. *Acta Crystallogr.* **1965**, *19*, 684−685.
(60) Cartz, L.; Srinivasa, S. R.; Riedner, R. J.; Jorgensen, J. D.; Worlton, T. G. Effect of Pressure on Bonding in Black Phosphorus. *J. Chem. Phys.* **1979**, *71*, 1718−1721.
(61) Akai, T.; Endo, S.; Akahama, Y.; Koto, K.; Marljyama, Y. The Crystal Structure and Oriented Transformation of Black Phosphorus under High Pressure. *High Pressure Res.* **1989**, *1*, 115−130.
(62) Ling, X.; Wang, H.; Huang, S.; Xia, F.; Dresselhaus, M. S. The renaissance of black phosphorus. *Proc. Natl. Acad. Sci. U.S.A.* **2015**, *112*, 4523−4530.
(63) Zhang, G.; Huang, S.; Wang, F.; Yan, H. Layer-Dependent Electronic and Optical Properties of 2D Black Phosphorus: Fundamentals and Engineering. *Laser Photonics Rev.* **2021**, *15*, 2000399.
(64) Zhang, C. D.; Lian, J. C.; Yi, W.; Jiang, Y. H.; Liu, L. W.; Hu, H.; Xiao, W. D.; Du, S. X.; Sun, L. L.; Gao, H. J. Surface Structures of Black Phosphorus Investigated with Scanning Tunneling Microscopy. *J. Phys. Chem. C* **2009**, *113*, 18823−18826.
(65) Li, L.; Kim, J.; Jin, C.; Ye, G. J.; Qiu, D. Y.; da Jornada, F. H.; Shi, Z.; Chen, L.; Zhang, Z.; Yang, F.; et al. Direct observation of the layer-dependent electronic structure in phosphorene. *Nat. Nanotechnol.* **2017**, *12*, 21−25.
(66) Zhou, Q.; Zhou, H.; Tao, W.; Zheng, Y.; Chen, Y.; Zhu, H. Highly Efficient Multiple Exciton Generation and Harvesting in Few-Layer Black Phosphorus and Heterostructure. *Nano Lett.* **2020**, *20*, 8212−8219.
(67) Joshi, P. P.; Li, R.; Spellberg, J. L.; Liang, L.; King, S. B. Nanoimaging of the Edge-Dependent Optical Polarization Anisotropy of Black Phosphorus. *Nano Lett.* **2022**, *22*, 3180−3186.
(68) Zhang, G.; Huang, S.; Chaves, A.; Song, C.; Özçelik, V. O.; Low, T.; Yan, H. Infrared Fingerprints of Few-Layer Black Phosphorus. *Nat. Commun.* **2017**, *8*, 14071.
(69) Zhou, J.; Cai, T.-Y.; Ju, S. Anisotropic Exciton Excitations and Optical Properties of Hittorf's Phosphorene. *Phys. Rev. Res.* **2020**, *2*, 033288.
(70) Margot, F.; Lisi, S.; Cucchi, I.; Cappelli, E.; Hunter, A.; Gutiérrez-Lezama, I.; Ma, K.; von Rohr, F.; Berthod, C.; Petocchi, F.; et al. Electronic Structure of Few-Layer Black Phosphorus from μ-ARPES. *Nano Lett.* **2023**, *23*, 6433−6439.
(71) Low, T.; Roldán, R.; Wang, H.; Xia, F.; Avouris, P.; Moreno, L. M.; Guinea, F. Plasmons and Screening in Monolayer and Multilayer Black Phosphorus. *Phys. Rev. Lett.* **2014**, *113*, 106802.